Fluid Dynamics &
Materials Processing

Tech Science Press

http://doi.org/10.32604/fdmp.2026.076988

ARTICLE

Control of Base Pressure in Supersonic Separated Flows over Axisymmetric Bodies Using Triangular Rib Actuators

Abdul Aabid[1,*], Renita Sharon Monis[2], Ambareen Khan[3], Sher Afghan Khan[4] and Muneer Baig[1]

[1]Department of Engineering Management, College of Engineering, Prince Sultan University, Riyadh, Saudi Arabia
[2]Department of Mathematics, Shri Madhwa Vadiraja Institute of Technology and Management (affiliated to VTU Belgaum), Bantakal, Udupi, India
[3]School of Aerospace Engineering, Tuanku Syed Sirajuddin Engineering Campus, Universiti Sains Malaysia, Nibong Tebal, Penang, Malaysia
[4]Department of Mechanical and Aerospace Engineering, Faculty of Engineering, IIUM, Kuala Lumpur, Malaysia
*Corresponding Author: Abdul Aabid. Email: aaabid@psu.edu.sa

Received: 30 November 2025; Accepted: 13 April 2026; Published: 27 May 2026

ABSTRACT: Separated flow at a blunt base remains a critical topic in both automotive and aerospace engineering, particularly in the context of high-speed and supersonic vehicles such as modern fighter aircraft. In the separated region, characterized by a recirculation zone, the local pressure is typically lower than the ambient back pressure. This reduced base pressure can account for up to 70 percent of the total drag acting on an axisymmetric body. The present study focuses on regulating the base pressure within the recirculation region to reduce base drag and thereby enhance the operational range of rockets, missiles, and related aerospace vehicles. The analysis considers key inertial and geometric parameters, including a Mach number of M = 1.8, different expansion levels, an area ratio of 6.25, and duct lengths ranging from L/D = 1 to 6. A triangular rib is introduced as a passive flow-control device to modulate the pressure within the duct. In the numerical simulations, the rib base is fixed at 3 mm, while its height varies from 1 mm to 5 mm. The results indicate that increasing the rib height enhances the base pressure, with the largest height producing the greatest pressure rise. A rib height of 3 mm is sufficient to raise the base pressure close to the back pressure. For applications requiring a more substantial increase in base pressure, ribs with heights of 4 or 5 mm are recommended, depending on mission constraints. Optimal performance is achieved when the rib is positioned at L/D = 3 or 4, where the maximum pressure gain is observed.

KEYWORDS: Triangular rib; base drag; compressible flow; steady flow; effect of area ratio

1 Introduction

Turbulent drag has significant financial and environmental impacts on engineering and real-world flows, primarily due to combustion by-products and the fossil fuels used by various forms of transportation, which account for more than 20% of overall emissions. Reducing turbulent drag will also help mitigate global warming by lowering CO_2 emissions from the burning of fossil fuels. Since near-wall turbulent structures significantly contribute to drag, efforts should be made to mitigate them. Passive and active control methods are the two main categories into which the techniques used to alter these near-wall structures can be roughly separated. Although it is simple to use passive techniques such as riblets, Gurney flaps, bleed, splitter plates, and super-hydrophobic surfaces, the drag reduction achieved is relatively small. Conversely, a significant reduction in skin-friction drag can be achieved with active control. However, searching for innovative active control approaches is alluring, even if implementing such techniques can be challenging and involve feedback loops.

Sudden expansion in internal flows typically generates a separated recirculation zone, a strong shear layer, and a significant reduction in base pressure. Previous studies have shown that separation and reattachment behaviour in expanding ducts is strongly influenced by geometry, expansion ratio, and turbulence characteristics [1,2]. Additional investigations have demonstrated that diffuser configuration and turbulence structure play a critical role in pressure recovery and vortex development [3,4]. In multiphase and compressible flow configurations, it has been reported that phase interactions and flow regime transitions significantly affect pressure fluctuations and energy dissipation in sudden expansions [5,6]. Arabi et al. [7,8] studied the identification of the Intermittent-flow sub-regime using pressure fluctuations. Further numerical and experimental studies on gas–liquid and gas–solid flows confirmed that sudden expansion critically governs pressure recovery mechanisms and overall flow stability [9–11].

In engineering applications, especially in nozzles, propulsion ducts, and supersonic internal flows, heat-transfer behavior, secondary vortices, and inlet conditions strongly affect performance [12]. At the same time, diffuser design and upstream parameters continue to determine pressure recovery and wall-heat transfer [13]. At high speeds, nozzle pressure ratio, gas temperature, and jet–shear–layer interaction directly influence base drag [14]. Reviews on flow-control strategies highlight the effectiveness of passive and active techniques, including ribs, cavities, contour shaping, and flow injection, in stabilizing shear layers and reducing drag [15]. Khan et al. [16] investigated how ribs act as passive control methods that affect base pressure for Mach 1. They found that flow regulation significantly increased base pressure by disrupting the recirculation sector and encouraging early flow reattachment. Exploring different rib shapes, Khan et al. [17] conducted simulations of Mach 1 flows, providing insights into velocity profiles and base-pressure changes. Research underscored the critical roles of nozzle geometry and expansion ratios in determining flow behavior.

Baig et al. [18] explored the use of base flows via microjets, demonstrating that active control methods can effectively manage base pressure and decrease drag. Rehman and Khan [19] devoted considerable attention to the use of micro-jets to control base pressure, offering valuable insights into the design and application of dynamic flow control methods. Rathakrishnan [20] conducted experiments using a converging nozzle followed by a sudden expansion at different primary pressure ratios, with three quadrilateral control mechanisms having w:h ratios of 3:1 to 3:3. He positioned five rectangular ribs inside a 12.5 mm-radius duct at 1D each. Outcomes indicated that for an aspect ratio (3:1), decreasing the base pressure, whereas a taller height of 3 mm tends to increase it. Also, the study conducted by Aabid and Khan [21] evidences that the CFD approach can solve such a problem of high-speed flow control.

Literature reviews indicate that at subsonic speeds, base drag accounts for nearly 10% of total viscous drag. At sonic Mach numbers, base drag becomes significant as the flow passes through a converging nozzle. For Mach numbers above unity, a converging-diverging nozzle is used, which is easier to fabricate than a Laval nozzle. Such nozzles are preferred for unguided rockets—area weapons that follow a fire-and-forget approach, whereas Laval nozzles are employed in guided missiles, which have a circular error probability of 0.1 percent. Laval nozzles are employed for guided aerospace launch vehicles due to their high precision. It is important to note that at the nozzle exit, three scenarios can occur: (i) over-expanded, (ii) correctly expanded, and (iii) under-expanded. In a CD nozzle, when the flow encounters adverse pressure, a strong shock forms at the nozzle lip, lasting until the pressure at that point matches the backpressure. When the nozzle is ideally expanded, the flow is assumed to be wave-free; however, Mach waves are observed around it. Additionally, within the region of these Mach waves, the flow remains isentropic.

From the above discussion, it is evident that there is a need to further explore the base pressure control study and its dependence on the inertia levels, Mach number, and area ratio when either static or dynamic control is employed. Further, no study has been conducted to control the base pressure in circular ducts at screech-prone Mach numbers and to assess the impact of flow management techniques.

2 Problem Definition

Sudden expansion in supersonic internal flows is known to generate strong flow separation, a large recirculation region, and a significant reduction in base pressure, which together contribute substantially to base drag and unsteady pressure fluctuations. These effects are particularly critical in aerospace propulsion systems, such as rocket nozzles and high-speed exhaust ducts, where increased base drag directly reduces overall propulsion efficiency and vehicle performance. Although both active and passive flow-control techniques have been proposed to mitigate these adverse effects, active control methods often require additional energy input and complex hardware, limiting their practical applicability. The present problem focuses on regulating the base pressure in a suddenly expanded duct under supersonic operating conditions using a simple passive control strategy. Specifically, the study investigates whether a triangular rib placed near the duct entrance can effectively modify the shear-layer development, recirculation behaviour, and pressure recovery downstream of a convergent–divergent nozzle operating at Mach 1.8. The problem is further extended to examine how rib height and axial location influence the flow response over a wide range of nozzle pressure ratios and duct length-to-diameter ratios.

Fig. 1 presents the baseline convergent–divergent nozzle and sudden-expansion duct geometry without any flow control, which serves as a reference configuration for evaluating inherent flow behaviour. Fig. 2 introduces triangular-rib configurations as a passive control mechanism. By systematically varying the rib height and position, the study aims to identify flow conditions and geometric parameters that yield maximum base-pressure recovery with minimal geometric modification. Addressing this problem is important for developing low-cost, passive solutions to base-drag reduction in high-speed internal flow applications.

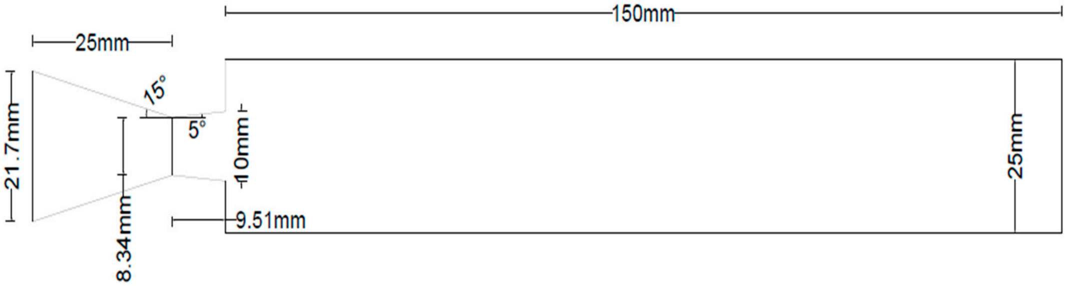

Figure 1: A complete geometry of the CD nozzle without the rib control.

3 CFD Method

The CFD simulations were performed using ANSYS FLUENT 2024/R2 to investigate the effect of triangular ribs as a passive control device on base-pressure behaviour, as illustrated in Figs. 1 and 2. Figs. 3 and 4 present the computational geometry and mesh configurations used in the study. Fig. 3 shows the baseline nozzle–duct configuration without ribs, while Fig. 4 depicts the rib-augmented cases, where triangular ribs of heights 1–5 mm are positioned downstream of the sudden expansion. In all cases, a structured mesh was employed, with local refinement near the sudden expansion corner, wall boundaries, and rib surfaces to accurately capture flow separation, shear-layer development, and reattachment behaviour.

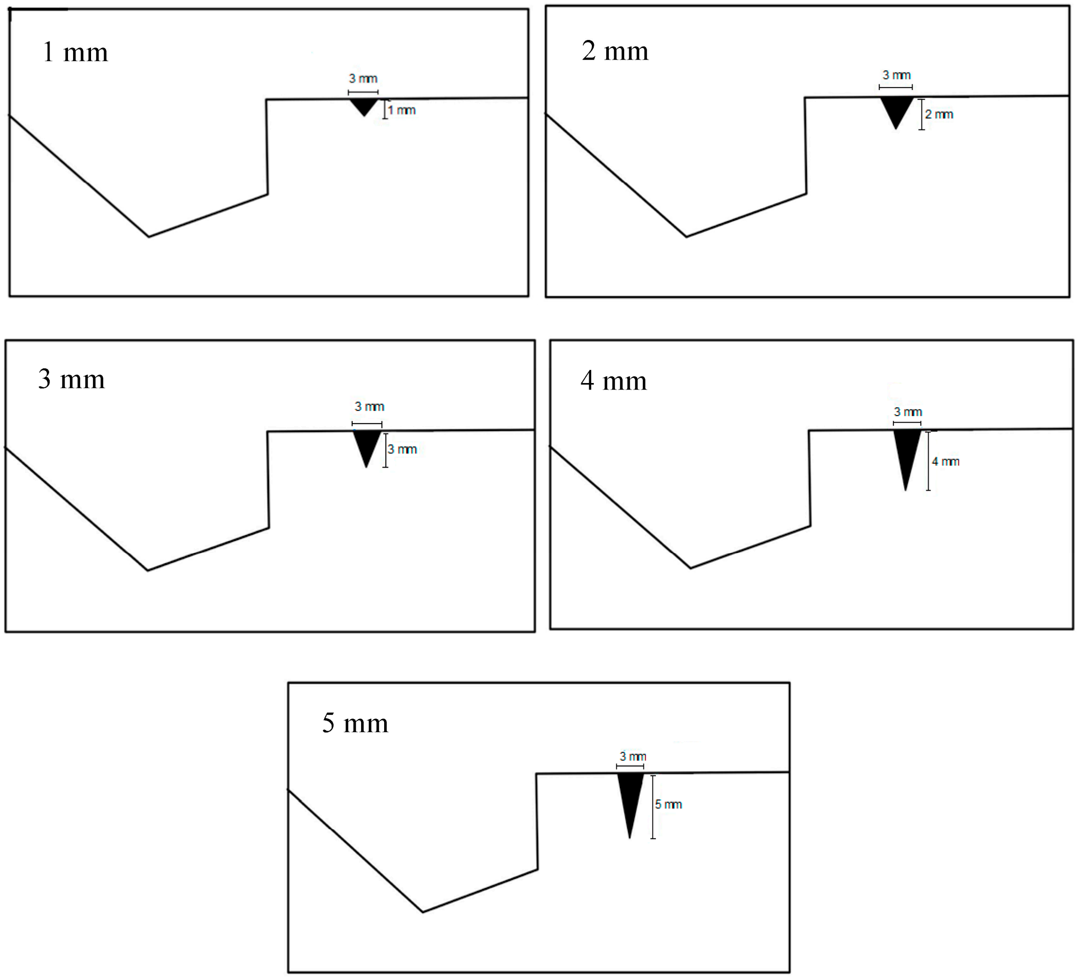

Figure 2: Nozzle and enlarged duct assembly with various triangular ribs.

Meshing was carried out for a two-dimensional axisymmetric model using a free-face structured meshing strategy. Element sizing was defined based on individual edge lengths to ensure uniform grid distribution along the nozzle contour and enlarged duct. Near-wall refinement was achieved using a biasing option with a bias factor of 10 to enhance mesh density close to solid boundaries and in regions of high flow gradients. Curvature-based sizing with a fine relevance center was also applied to preserve geometric fidelity and improve numerical stability. Mesh quality was evaluated using standard metrics, and the resulting skewness and element-quality values were found to be within the limits recommended by ANSYS Fluent. Consistent mesh quality was maintained across all rib configurations.

A pressure inlet corresponding to the prescribed nozzle pressure ratio (NPR) was specified at the nozzle inlet, while a pressure outlet with atmospheric pressure was imposed at the duct exit. All solid surfaces, including the nozzle, duct, and rib walls, were treated as no-slip adiabatic boundaries, and an axisymmetric condition was applied along the centreline. These boundary conditions were kept identical for all cases to ensure a fair comparison of rib-height and rib-location effects.

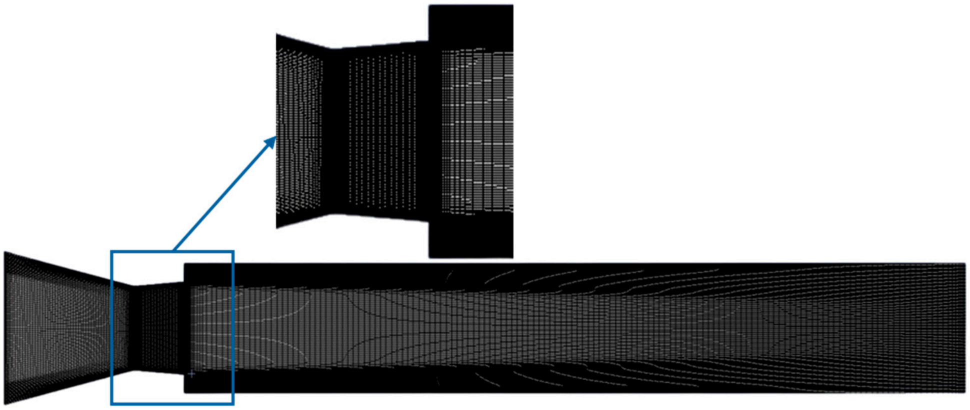

Figure 3: Nozzle and duct without the triangular ribs.

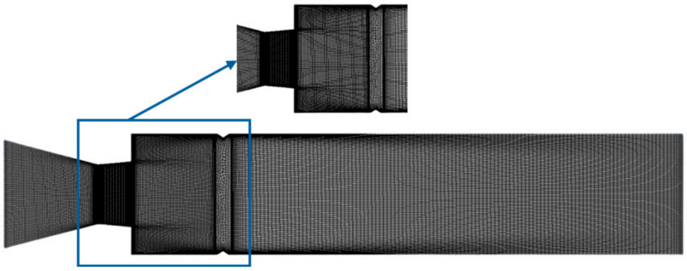

(**a**)

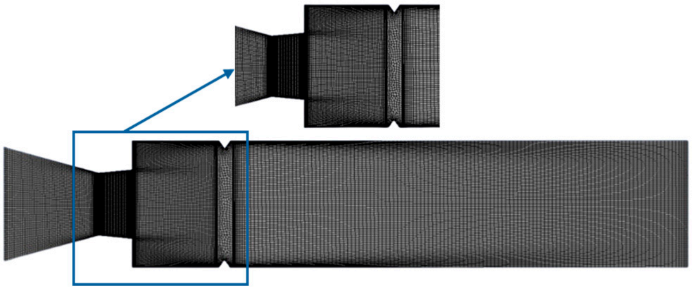

(**b**)

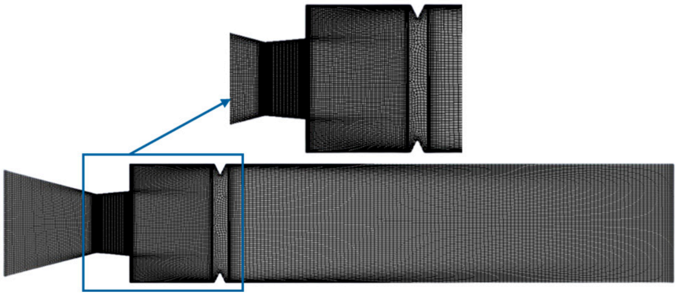

(**c**)

Figure 4: *Cont.*

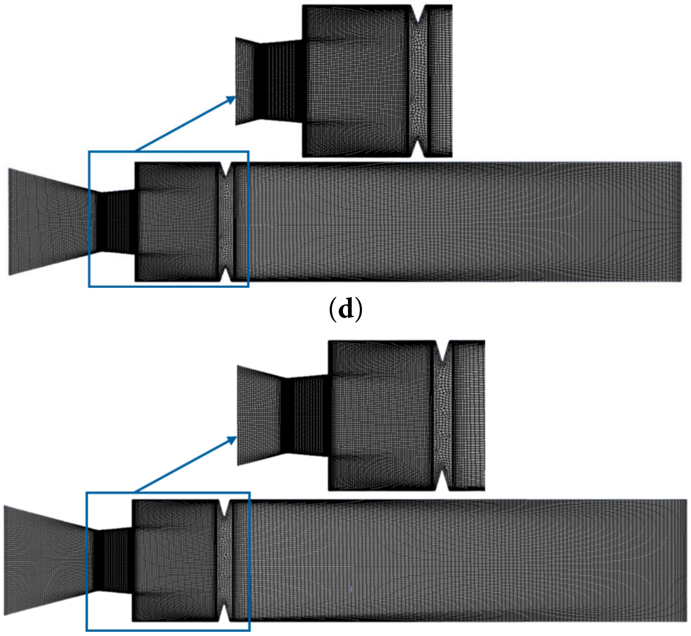

(**d**)

(**e**)

Figure 4: Nozzle and duct with triangular ribs of (**a**) height 1 mm, (**b**) 2 mm, (**c**) 3 mm, (**d**) 4 mm, and (**e**) 5 mm.

3.1 CFD Flow Conditions and Simulation Parameters

To reproduce the flow behavior under realistic operating conditions while maintaining numerical efficiency, appropriate physical assumptions were adopted. These assumptions define the simulation framework and are consistent with the flow conditions summarized in Table 1.

i. The flow is assumed to be steady, two-dimensional, and axisymmetric, which is appropriate for the present CD nozzle and sudden-expansion duct geometry and allows accurate prediction of the dominant flow features with reduced computational cost.
ii. Air is treated as a compressible ideal gas, and density variation is accounted for. A pressure inlet condition is prescribed at the nozzle inlet based on the nozzle pressure ratio (NPR = 3–11), corresponding to a design Mach number of M = 1.8, while a pressure outlet at atmospheric pressure is imposed at the duct exit.
iii. The flow is considered fully turbulent, and turbulence plays a significant role in governing shear-layer growth, recirculation, and base-pressure behavior in the sudden-expansion region. Accordingly, the flow field is modelled using the standard $k-\varepsilon$ turbulence model, which has been widely validated for high-speed internal flows.
iv. The viscosity of air is assumed to be temperature-dependent, enabling accurate representation of compressible flow effects associated with expansion and shock interactions.
v. All solid boundaries, including the nozzle walls, enlarged duct walls, and rib surfaces, are treated as no-slip adiabatic walls, while an axisymmetric boundary condition is applied along the centreline. These boundary conditions are kept identical across all cases to ensure a fair comparison of the effects of rib height, rib location, and duct length.

Under these assumptions, the selected Mach number, NPR range, area ratio, and duct length ratios (L/D = 1–6), as summarized in Table 1, span the over-expanded, ideally expanded, and under-expanded regimes. This provides a consistent and systematic framework for evaluating base-pressure behavior and assessing the effectiveness of triangular ribs as a passive flow-control technique.

Table 1: Flow conditions and simulation parameters used in the present study.

Parameter	**Value/Range**	**Description**
Flow type	Steady, compressible, turbulent	Supersonic internal flow through a CD nozzle with sudden expansion
Flow model	2D axisymmetric	Geometry and flow are assumed axisymmetric
Working fluid	Air (ideal gas)	Temperature-dependent viscosity
Mach number (M)	1.8	Design Mach number at nozzle exit
Nozzle pressure ratio (NPR = P_0/Pa)	3–11	Covers over-expanded, ideally expanded, and under-expanded regimes
Area ratio (A_2/A_1)	6.25	Ratio of enlarged duct area to nozzle exit area
Duct length ratio (L/D)	1–6	Represents short to long enlarged duct configurations
Rib type	Triangular (passive control)	Fixed rib base width of 3 mm
Rib height (h)	1–5 mm	Investigated to assess passive control effectiveness
Rib axial location	0.5D–4D	Measured from the sudden expansion plane
Inlet boundary condition	Pressure inlet	Total pressure set based on NPR
Outlet boundary condition	Pressure outlet (Pa)	Atmospheric pressure
Wall condition	No-slip, adiabatic	Applied to nozzle, duct, and rib surfaces
Turbulence model	Standard k–ε	Used for all simulations
Solver	Pressure-based, steady	ANSYS FLUENT 2024/R2

3.2 Numerical Solver Settings and Turbulence Modelling

The flow conditions, geometric parameters, and boundary conditions employed in the present CFD study are summarized in Table 1 and discussed in Section 4.1. This section provides additional details on the numerical solver settings, turbulence modelling approach, near-wall treatment, and discretization schemes used in the simulations. All simulations were carried out using ANSYS FLUENT 2024/R2 with a pressure-based, steady-state solver, chosen for its robustness in predicting compressible internal flows with shock–shear-layer interactions and flow separation. The governing equations for mass, momentum, energy, and turbulence quantities were solved in a segregated manner with pressure–velocity coupling handled using the SIMPLE algorithm.

Turbulence effects were modelled using the standard k–ε turbulence model, which has been widely adopted for high-speed internal flows involving sudden expansion, recirculation, and reattachment. Standard wall functions were employed for near-wall turbulence treatment. The computational mesh was designed to maintain dimensionless wall distance (y+) values predominantly within the 30–150 range, which is appropriate for the selected turbulence model and wall-function approach.

Second-order upwind discretization schemes were applied for momentum, energy, and turbulence transport equations to reduce numerical diffusion and improve solution accuracy. Convergence was ensured by reducing residuals to 10^{-4} for the continuity, momentum, and turbulence equations, and 10^{-6} for the energy equation, while monitoring the stabilization of base-pressure values. All solver controls, numerical schemes, and turbulence parameters were kept identical for all cases, ensuring numerical consistency and enabling a fair comparison of rib height, rib location, and duct length effects on base-pressure behavior.

3.3 Validation of CFD Method

To validate the accuracy and reliability of the present CFD work, a direct comparison was carried out with the experimental data reported by Rehman and Khan [19], who investigated base-pressure control using micro-jets for a sudden expansion flow. Fig. 5 presents a predicted variation of the non-dimensional base pressure ratio (Pb/Pa) with NPR, comparing the present CFD results against the experimental measurements for NPR values ranging from 3 to 11.

The comparison shows that the present numerical predictions closely follow the experimental trends for all NPRs considered. At lower NPRs (3 to 5), where the flow is strongly over-expanded and shock–shear-layer interactions dominate the base region, the CFD results slightly under-predict the base pressure compared to the experiments. This deviation is expected and has been reported in earlier studies, as experimental measurements inherently include unsteady effects, small-scale turbulence, and flow asymmetries that are not fully captured in steady RANS simulations. As NPR increases beyond 5, the agreement between CFD and experimental results improves significantly. In this regime, the nozzle flow transitions toward ideal and under-expanded conditions, and the predicted base pressure values align closely with the experimental data for NPR = 7, 9, and 11. The CFD model successfully reproduces the gradual recovery of base pressure with increasing NPR, confirming that the numerical setup, turbulence modelling, and boundary conditions accurately capture the dominant flow physics governing base pressure behavior.

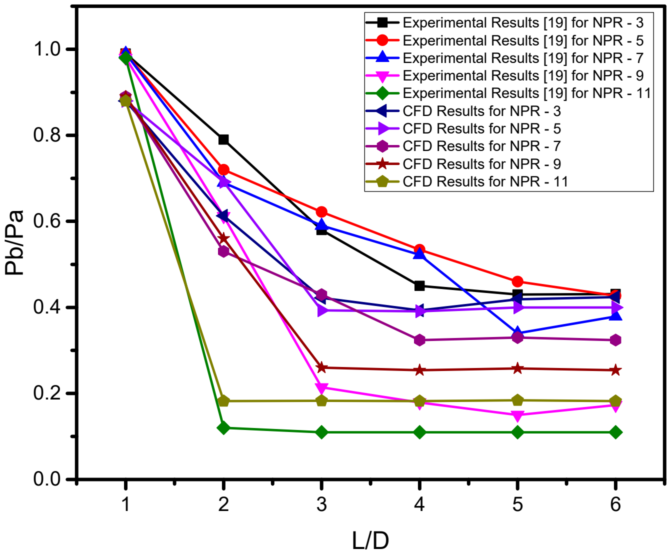

Figure 5: Comparison and validation of the CFD method.

3.4 Mesh Convergence Test

Table 2 presents the mesh independence analysis by combining the mesh characteristics (number of nodes and elements) with the corresponding wall-pressure ratio (P_w/P_a) obtained at different NPR values. It is observed that the pressure predictions vary noticeably between the coarser grids, whereas the difference becomes progressively smaller as the mesh is refined. From the fine grid onwards, the variation in (P_w/P_a) is minimal, indicating that further refinement has a negligible effect on the solution. This confirms that the selected mesh is sufficiently fine to ensure grid-independent results while maintaining computational efficiency.

Table 2: Mesh independence analysis, including mesh details and pressure variation (P_w/P_a).

Grid Level	Nodes	Elements	NPR = 3	NPR = 5	NPR = 7	NPR = 9	NPR = 11
Coarsest	2992	2816	0.31	0.21	0.26	0.33	0.41
Coarse	3866	3660	0.30	0.20	0.25	0.32	0.40
Medium 1	9371	9066	0.29	0.19	0.24	0.31	0.39
Medium 2	16,944	16,553	0.28	0.18	0.22	0.28	0.34
Fine	104,586	103,691	0.25	0.16	0.21	0.27	0.33
Finer	297,362	295,870	0.22	0.15	0.20	0.26	0.32
Finest	1,472,692	1,469,434	0.21	0.14	0.20	0.25	0.31

Fig. 6 shows the variation of the non-dimensional base pressure with NPR for different mesh densities. Although minor variations in base-pressure values persist with increasing mesh refinement, the results exhibit a clear trend toward stabilization beyond the fine-mesh level. For meshes finer than the selected fine configuration, additional refinement produces only marginal changes in the predicted base pressure, while the overall trends and relative differences between NPR cases remain unchanged. It is important to note that the present flow involves shock–shear layer interaction, separation, and recirculation in a sudden-expansion duct, which are inherently sensitive to grid resolution. In such flows, strict asymptotic convergence to a single constant value is rarely observed. Instead, mesh independence is established when further grid refinement leads to negligible changes in the quantities of interest relative to the required engineering accuracy. In the present study, the variation in base pressure between the fine and finer meshes remains within an acceptable tolerance, whereas the computational cost increases significantly for the finest mesh. Therefore, the fine mesh was selected as an optimal compromise between numerical accuracy and computational efficiency, and all parametric simulations were conducted using this mesh to ensure consistency across cases.

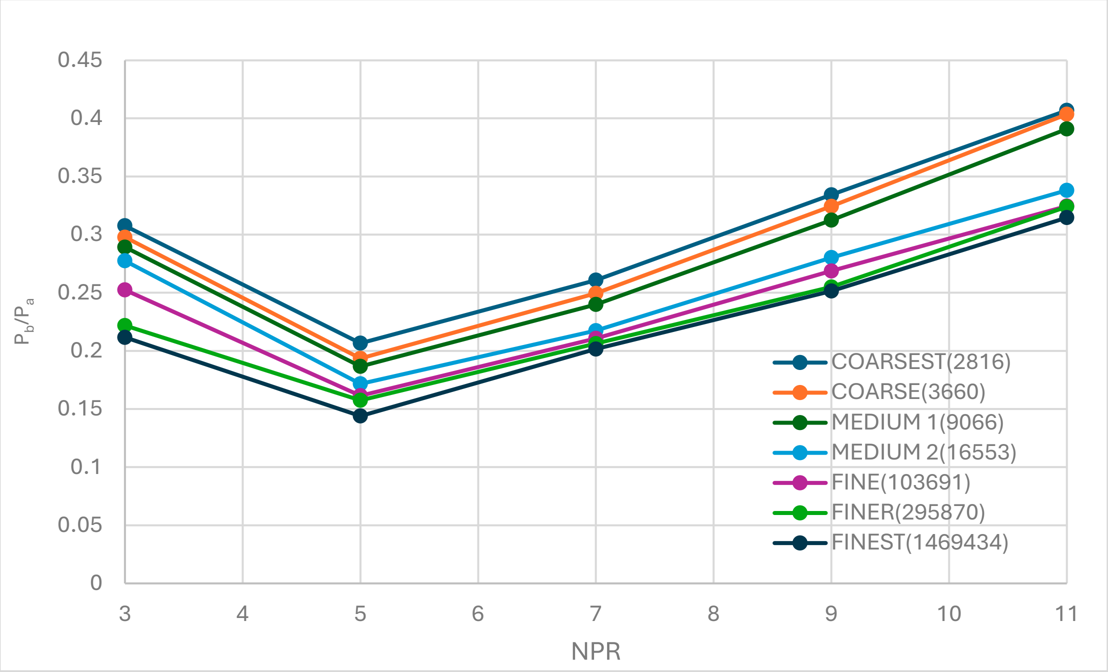

Figure 6: Mesh independent test.

4 Results and Discussion

This study focuses on base pressure control using a triangular rib, with the rib base fixed at 3 mm and the rib height varying from 1 to 5 mm for NPRs from 3 to 11. Due to variations in expansion levels, there will be a progressive decline in over-expansion. Ideally, the expansion will dictate the formation of the shockwaves at the nozzle lip, and as NPRs increase further, the nozzle flow will become under expanded. The ribs were placed in the duct at various locations, with L/D ranging from 0.5 to 4 (i.e., at 12.5 mm, 25 mm, 37.5 mm, 50 mm, 75 mm, and 100 mm from where the enlarged duct starts. Since the duct has a radius of 12.5 mm, the flow is expected to reattach approximately 75 mm downstream of the CD nozzle exit, with a design Mach number of 1.8 at the nozzle exit plane. The simulation results were converted to absolute pressure by accounting for backpressure and then standardized by dividing them by the backpressure. This Mach number, M = 1.8, was selected just to ascertain the impact of passive control at a screech-prone Mach number.

4.1 Selected Contours: Flow Formation near the Sudden Expansion Duct

The flow-field samples presented in Table 3 illustrate the representative behavior of the sudden-expansion duct when a triangular rib is positioned 19 mm from the base (0.5D downstream of the expansion plane) for NPR = 3 and L/D = 1. For each rib height (1–5 mm), streamline patterns, velocity contours, and pressure contours are shown to provide a comprehensive description of the flow evolution and the associated passive-control effects. The streamline contours reveal the development and modification of the recirculation region downstream of the sudden expansion. As the rib height increases, the size and structure of the recirculation zone are noticeably altered, indicating enhanced interaction between the shear layer and the rib-induced disturbances.

The velocity contours further demonstrate how the jet-core spreading and shear-layer growth evolve with increasing rib height. Although the rib modifies the near-wall flow and recirculation characteristics, the core jet retains relatively high inertia, particularly for larger rib heights, indicating that the rib primarily influences the separated region rather than completely suppressing the jet momentum. The pressure contours complement the streamline and velocity results by highlighting the pressure redistribution caused by the rib. An increase in rib height leads to stronger local pressure gradients near the rib and along the reattachment region, confirming the rib's role in modifying the pressure recovery process in the enlarged duct. These combined contours collectively demonstrate the interaction among velocity reduction, pressure rise, and flow reattachment. Although the complete numerical investigation covered five rib heights, six duct-length ratios (L/D = 1–6), and nine nozzle pressure ratios (NPR = 3–11), resulting in more than 100 possible contour plots, only the representative cases shown in Table 1 are included. Presenting all contour combinations would excessively increase the manuscript length and reduce clarity without providing additional physical insight.

The selected cases are sufficient to demonstrate numerical stability, mesh and solver reliability, and the effectiveness of the rib placed at 0.5D in modifying the flow structure as shown in Table 3. When the rib is located 19 mm from the nozzle exit, the flow remains transitional and developing, as the shear layer continues to expand within the enlarged section. Once the flow fully reattaches to the duct wall, the resulting patterns represent the actual flow behavior in the sudden-expansion region. Overall, the combined streamline, velocity, and pressure contours confirm that increasing rib height significantly influences the recirculation and pressure recovery characteristics, while the main jet preserves a high-momentum core.

Table 3: Flow formation for the rib is placed 19 mm from the base, NPR 3, L/D = 1.

Rib Size	Streamlines Contours	Velocity Contour	Pressure Contour
1 mm	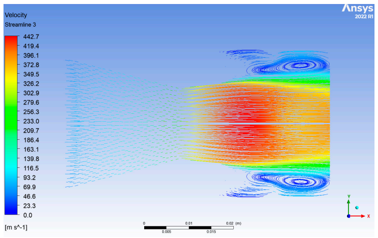	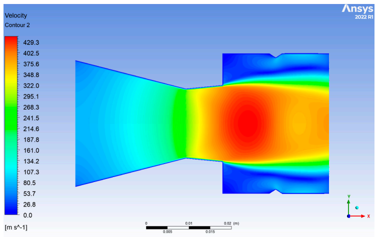	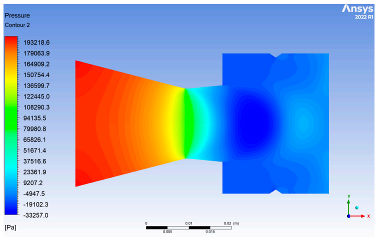
2 mm	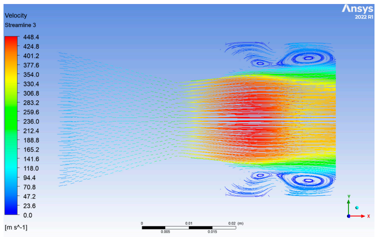	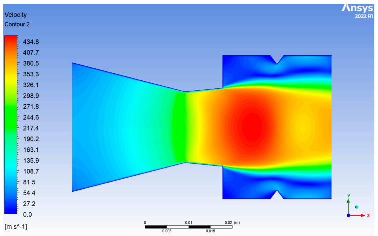	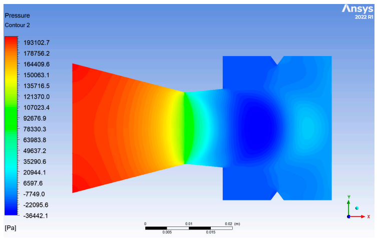
3 mm	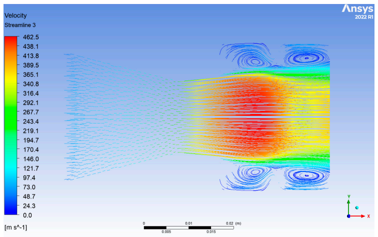	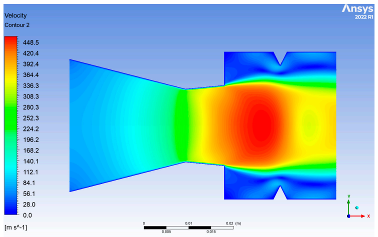	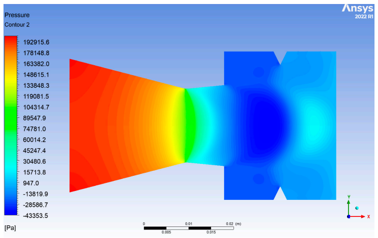
4 mm	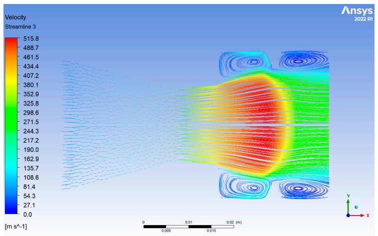	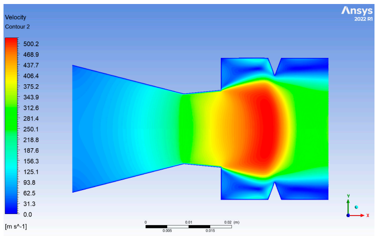	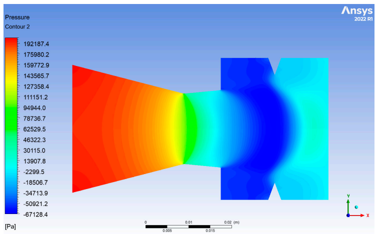
5 mm	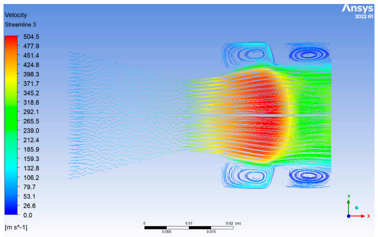	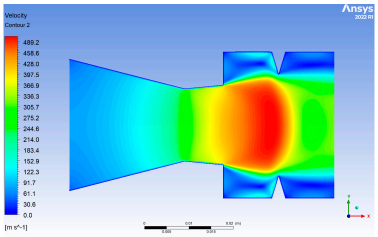	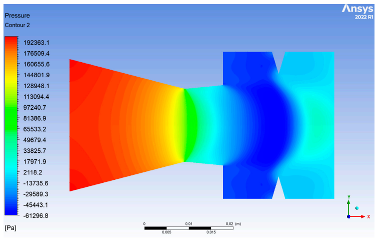

4.2 Base Pressure Findings for Rib Position at L/D = 0.5

Fig. 7 displays the outcomes of this investigation for a triangular rib with L/D = 0.5 (19 mm from the nozzle exit). Simulations were conducted for NPRs 3 to 11, rib heights 1 mm to 5 mm in increments of 1 mm, and duct dimensions from L/D = 1 to 6. Results show that without control at NPR = 3, the base pressure ratio is very high. There is a progressive decrease in its value till the nozzle flow remains over-expanded. Once the nozzle reaches the NPR required for ideal expansion, the decreasing trend stops. For NPR > 5, the base pressure increases. The literature shows that when the nozzle is over-expanded, a powerful shock forms at the exit plane, and this process of shock formation and interaction continues until the jet pressure equals the ambient pressure. Some oscillations are also observed; these may be due to interactions between the oblique shock waves and the dividing streamline, as well as with the base vortex.

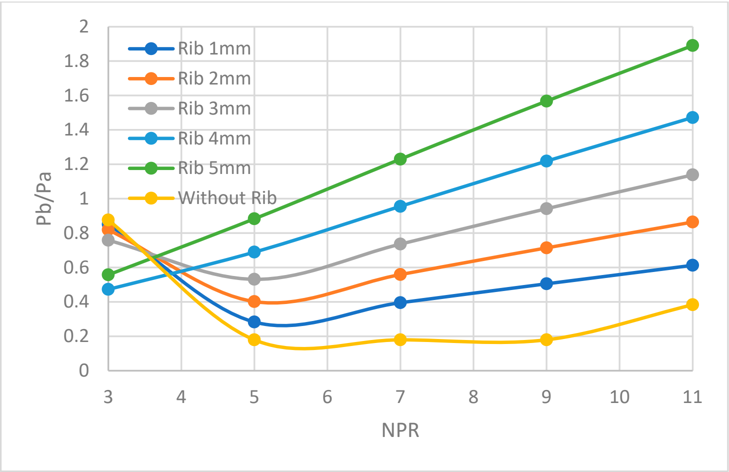

(**a**) L/D = 1

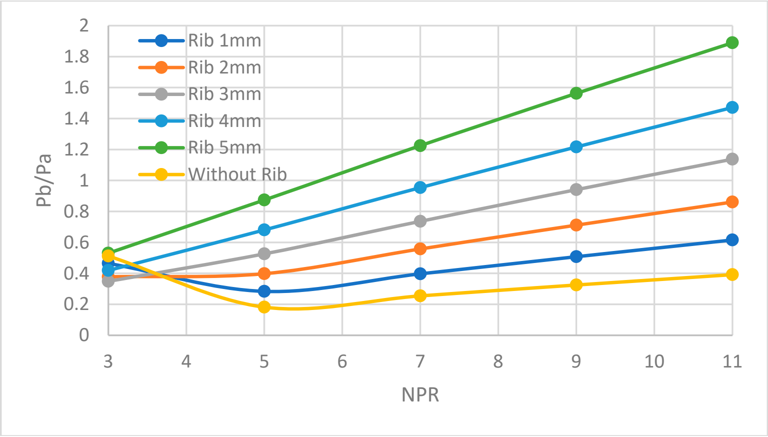

(**b**) L/D = 2

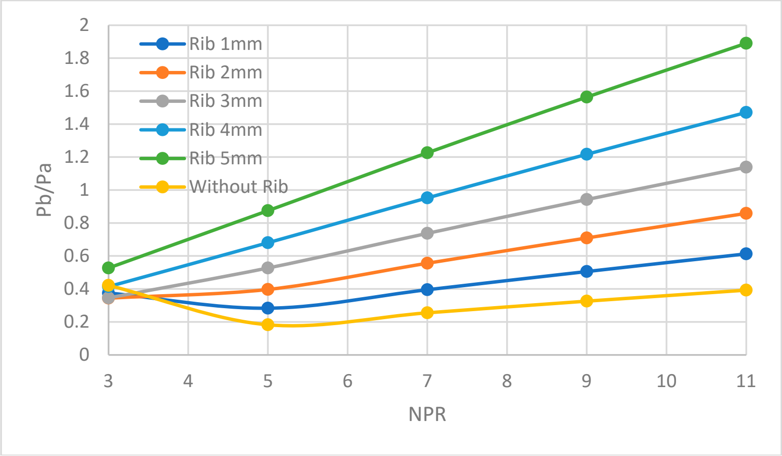

(**c**) L/D = 3

Figure 7: *Cont.*

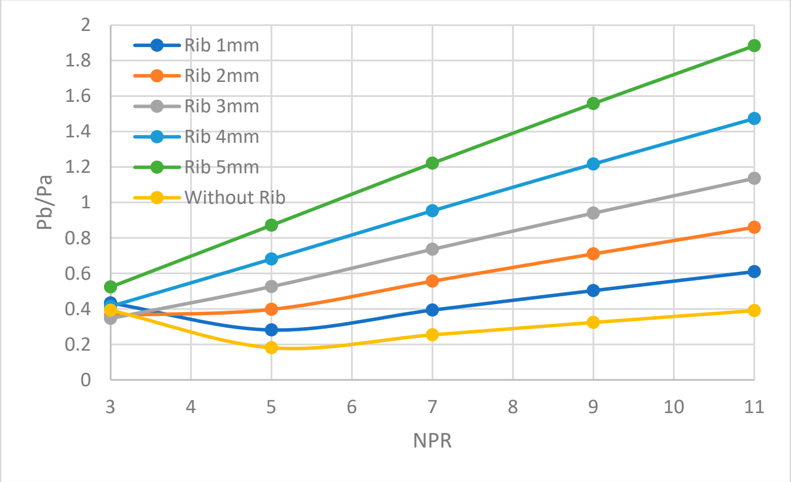

(**d**) L/D = 4

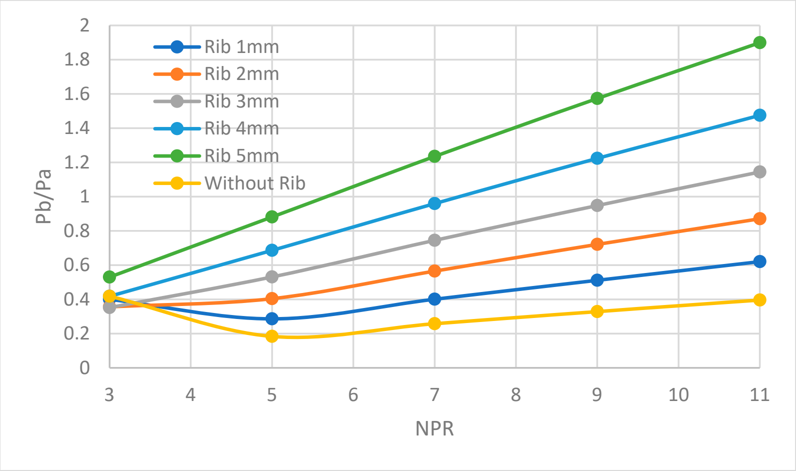

(**e**) L/D = 5

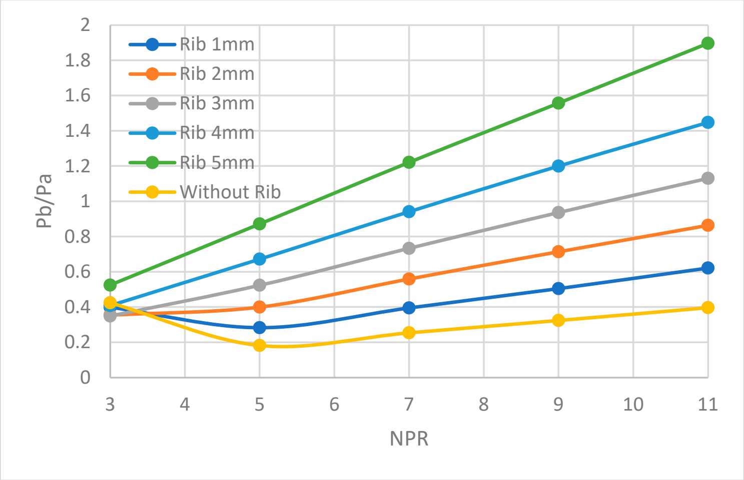

(**f**) L/D = 6

Figure 7: Base pressure ratio vs. NPR at different rib heights, rib location at L/D = 0.5, and the duct lengths. (**a**) L/D = 1, (**b**) L/D = 2, (**c**) L/D = 3, (**d**) L/D = 4, (**e**) L/D = 5, (**f**) L/D = 6.

When control is employed as a triangular rib with a 3 mm base and a height varying from 1 mm to 5 mm, the base pressure increases considerably for a one mm-height rib. Nevertheless, the decreasing trend in base pressure persisted, as seen in the absence of control. With an increase in rib altitude of 1–3 mm, the base pressure results show a linear growth. Conversely, the trends in base pressure at rib altitudes of 4 mm and 5 mm differ. At NPR 3, strong suction is created, and as NPR increases, the base pressure rises linearly. There is a substantial rise in the base pressure. The base suction at the NPR = 3 is related to the altitude of the rib and, hence, the resulting blockage to the flow. At NPRs > 3, there was a direct increase of the base pressure, with resulting base pressure values of 1.5 and 1.9; however, this trend is within the expected range.

Since these results pertain to the rib position with L/D = 0.5, which is far from the reattachment point, the flow remains transitional. Therefore, these results do not represent the actual flow conditions. Hence, we look for the rib's other location rather than this placement. Furthermore, a minor change in base pressure occurs at L/D = 2. Owing to the decreased impact of the backpressure. For the remaining duct sizes, the base pressure results do not change significantly, and similar results are observed for duct sections with L/D ranging from 3 to 6.

4.3 Base Pressure Findings for Rib Position at L/D = 1.0

While the rib is established at L/D = 1.0, the base pressure estimates are shown in Fig. 8 for various expansion levels and duct dimensions. The effect of a 1 mm rib height is nearly absent, except when the nozzle is facing an adverse or favorable pressure gradient. This tendency in the base pressure and the rib's ineffectiveness can be attributed to the resulting flow field, the rib's interaction with the viscous layer, and the reverse flow induced by the secondary vortices formed at the rib's sharp corner. The findings show that for the lower rib heights, namely h = 2 mm, 3 mm, and 4 mm, the results are nearly the same as those for rib placement at L/D = 0.5. It appears that, for rib placement at L/D = 1.0 and rib heights ranging from 1–4 mm, they do not lead to considerable growth in base pressure, as seen in Fig. 8a. It may be due to the reattachment position and backpressure. However, at a rib altitude of 5 mm, we observe a meaningful rise in base pressure, among other effects. Hence, the base pressure is maximum for the duct segments L/D = 2 and 6. This rise in base pressure can be attributed to the circumstance that, at L/D = 2, ambient pressure has a significant influence on base pressure. When L/D = 6, the duct's considerable span completely negates the effect of ambient pressure, and the long duct length determines the maximum base pressure.

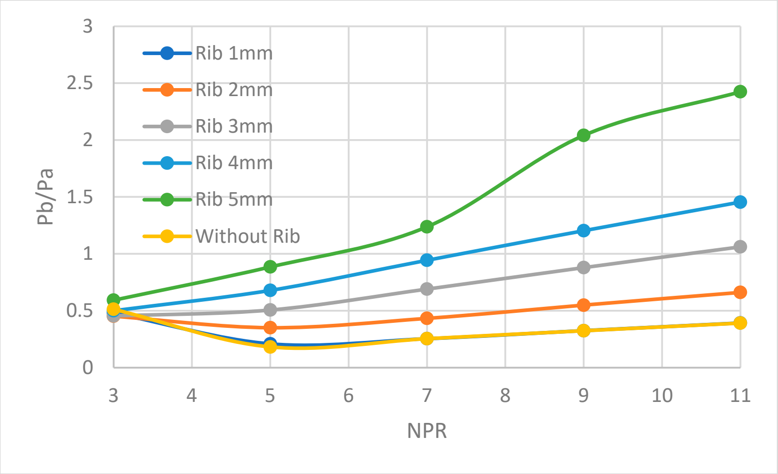

(**a**) L/D = 2

Figure 8: *Cont.*

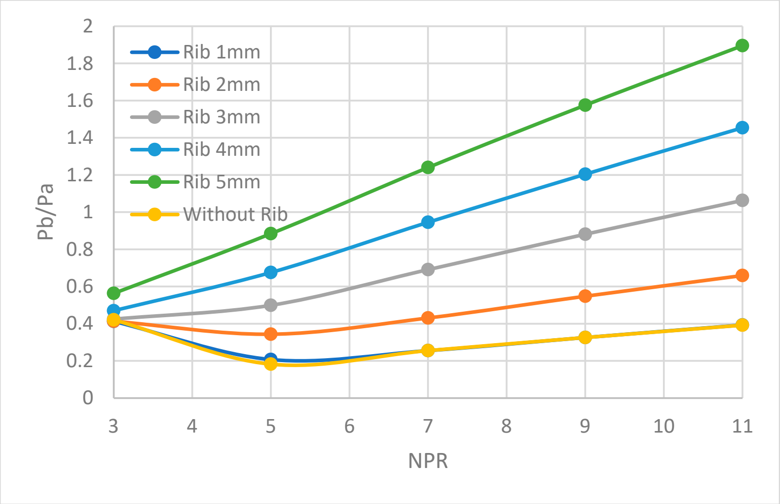

(**b**) L/D = 3

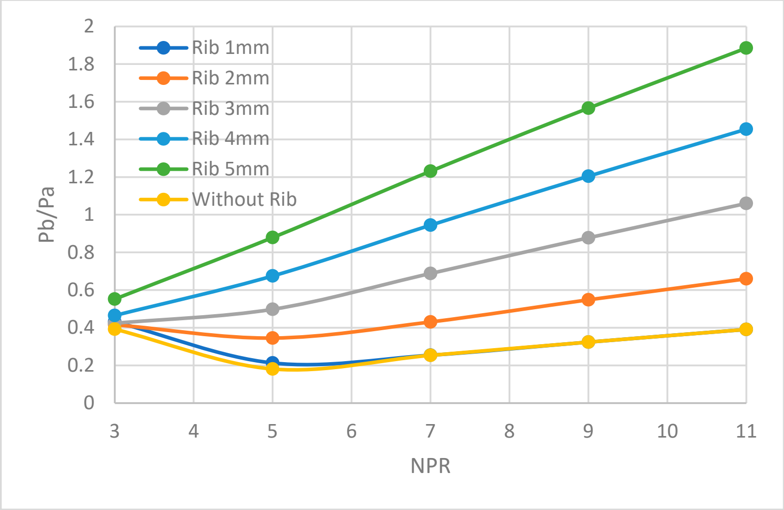

(**c**) L/D = 4

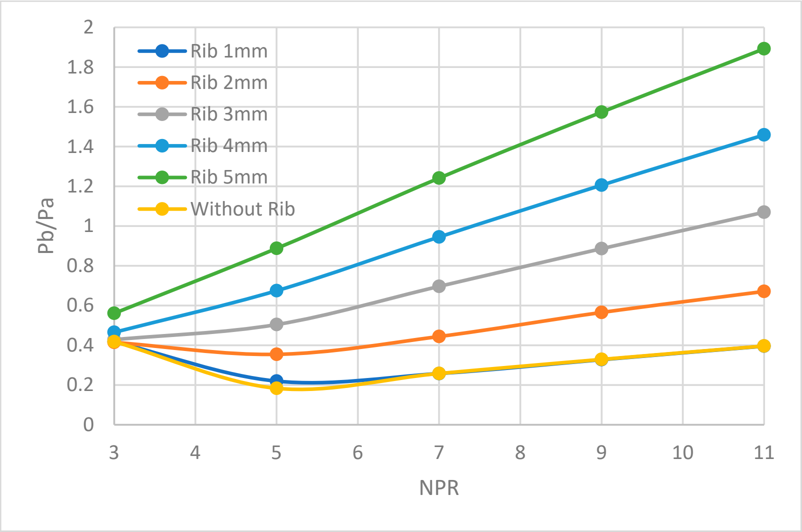

(**d**) L/D = 5

Figure 8: *Cont.*

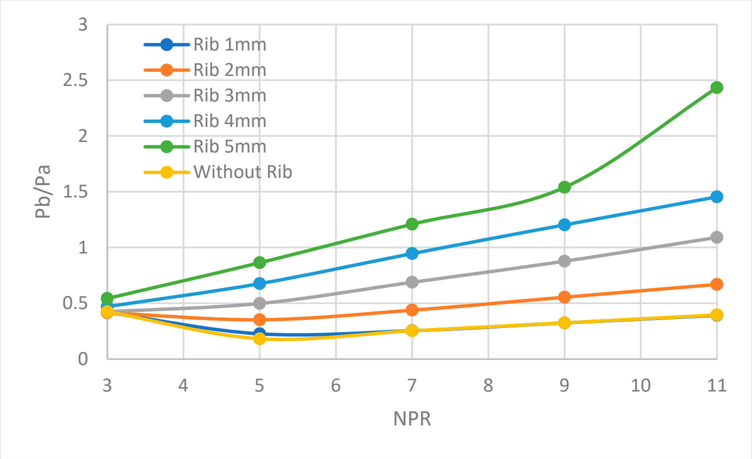

(**e**) L/D = 6

Figure 8: Base pressure ratio vs. NPR at different rib heights, rib location at L/D = 1.0, and the duct lengths. (**a**) L/D = 2, (**b**) L/D = 3, (**c**) L/D = 4, (**d**) L/D = 5, (**e**) L/D = 6.

4.4 Base Pressure Findings Once the Rib Position at L/D = 1.5

The base pressure at the rib position for L/D = 1.5 is shown in Fig. 9, with a greater change in the rib locations in the downstream direction for NPRs varying between 3 and 11 in duct segments with L/D ratios from 1 to 6. This additional change in rib position near the downstream end increases base pressure at rib altitudes of 2 to 5 mm, as shown in Fig. 9a. The efficacy of a rib with 1 mm height remains marginal for NPRs in the range of NPR = 3 to 6. For the remaining NPRs tested, the passive control, triangular rib, shows no improvement. As for the other ribs, with heights ranging from 2 to 4 mm, a substantial increase in base pressure is observed across all duct lengths; however, for tube segments with L/D = 2 & 3, no increase in base pressure is observed due to the increase in duct span. It is also noted that for L/D = 4 & a rib height of 3 mm, the base pressure increases; for the remaining duct dimensions, up to L/D = 5, the base pressure remains unchanged. For a tube with L/D = 6, the base pressure decreases insignificantly. This change in base pressure is attributed to the tube's maximum length, and the back pressure cannot alter the flow within the duct.

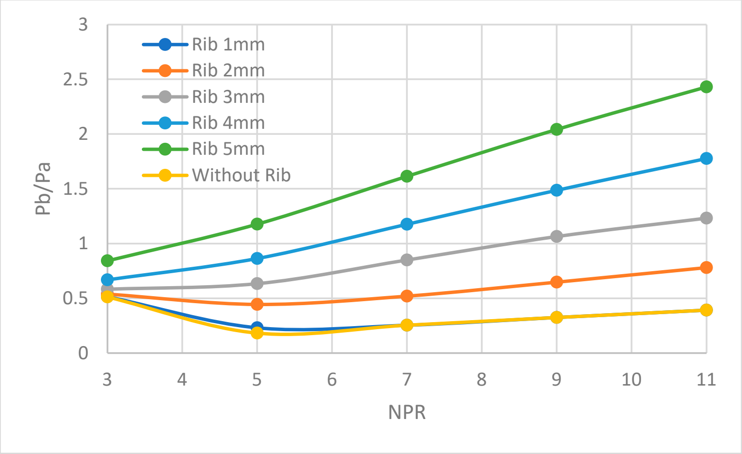

(**a**) L/D = 2

Figure 9: *Cont.*

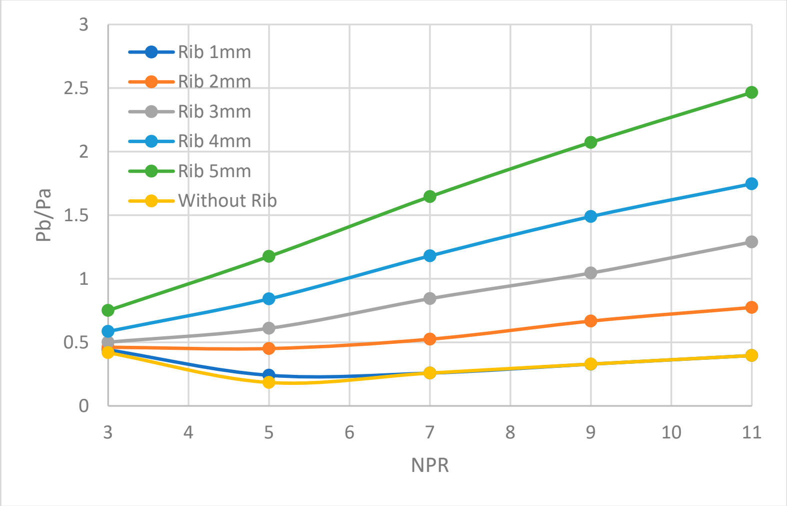

(**d**) L/D = 5

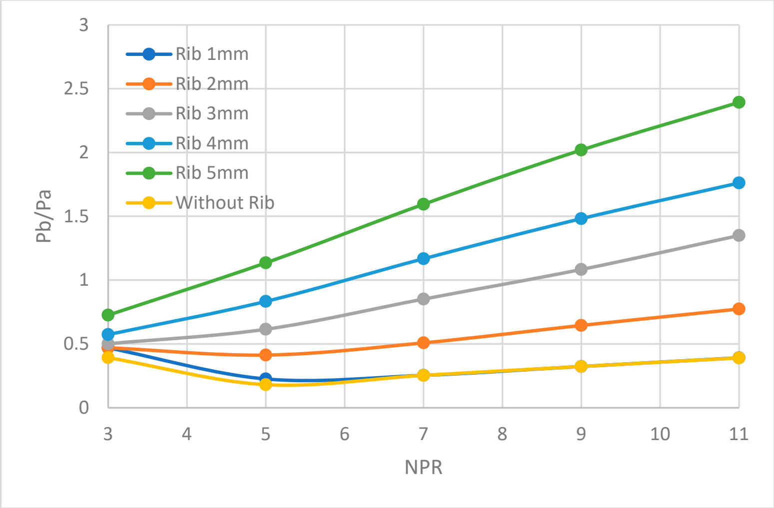

(**c**) L/D = 4

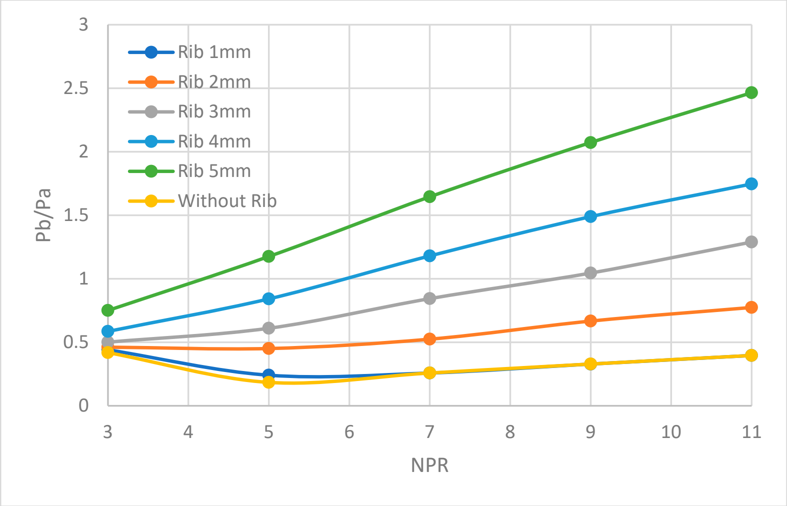

(**d**) L/D = 5

Figure 9: *Cont.*

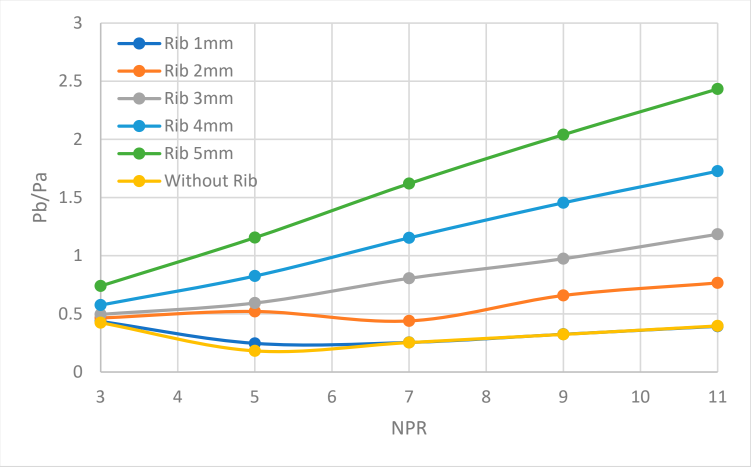

(**e**) L/D = 6

Figure 9: Base pressure ratio vs. NPR at different rib heights, rib location at L/D = 1.5, and the duct lengths. (**a**) L/D = 2, (**b**) L/D = 3, (**c**) L/D = 4, (**d**) L/D = 5, (**e**) L/D = 6.

4.5 Base Pressure Outcomes for Rib Position at L/D = 2.0

Fig. 10 illustrates the results of the present analysis for a triangular rib at L/D = 2.0 in the duct. Simulations were conducted for NPRs ranging from 3 to 11 and for duct segments with L/D ratios from 1 to 6. From the figure, it is seen that when the rib height is 1 mm, and the NPRs range from 3 to 6, the nozzle experiences either an adverse or a favorable pressure. For highly under-expanded nozzles, the rib is ineffective. Similarly, for a 2 mm rib height, there is no significant difference in control effectiveness amongst the rib placements, namely L/D = 0.5 to 1.5. Nonetheless, when the rib altitudes vary by 3 to 5 mm, control effectiveness changes significantly compared to lower heights, and the base pressure reaches 1.5, 2.1, and 3.0, which are substantial. These increases occur because, as rib height increases, air from the main jet is transferred to the base recirculation zone, thereby increasing base pressure. Furthermore, the formation of secondary vortices also increases pressure in the recirculation zone, as shown in Fig. 10a. Analogous findings are observed in the continuing duct segments, where the base pressure remains constant and shows only marginal changes. These changes may be due to the increased length of the tube segment, as the base pressure is not influenced by backpressure, unlike in smaller duct segments.

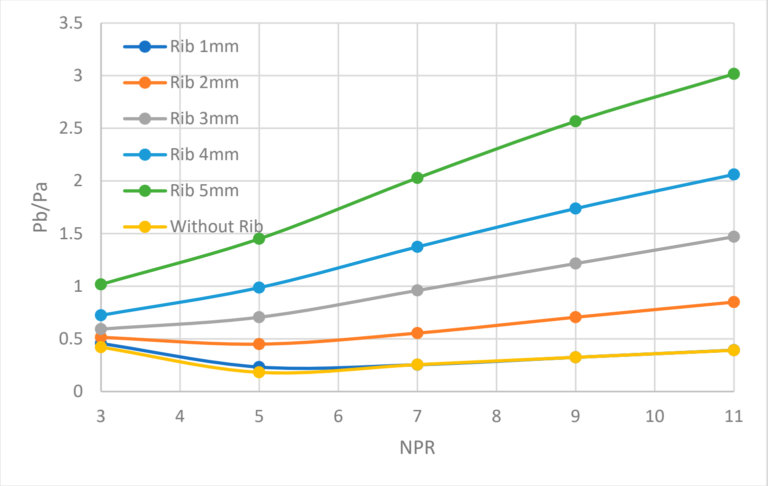

(**a**) L/D = 3

Figure 10: *Cont.*

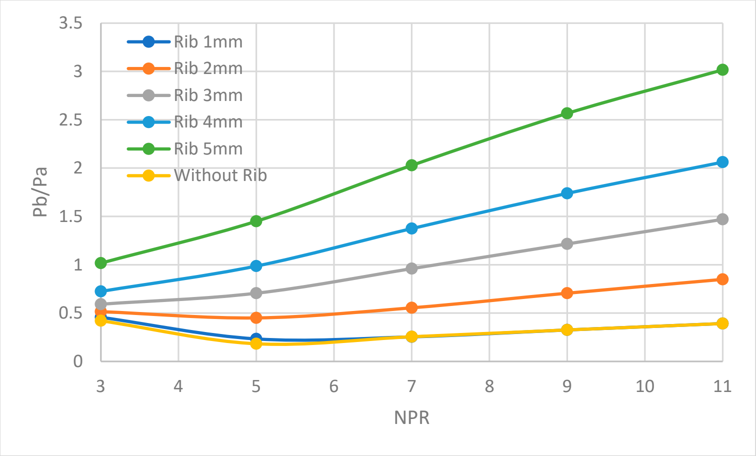

(**b**) L/D = 4

Figure 10: Base pressure ratio vs. NPR at different rib heights, rib location at L/D = 2.0, and duct lengths. (**a**) L/D = 3, (**b**) L/D = 4.

4.6 Base Pressure Outcomes for Rib Position at L/D = 3.0

At L/D = 3.0, the findings are shown in Fig. 11 for different expansion levels, tube segments, and rib heights. Regarding the effectiveness of control across multiple locations and rib heights, this location appears optimal. For a tube radius of 12.5 mm, reattachment appears to occur in the range L/D = 3–4, with most cases near L/D = 3. The physics of this tendency may be that when the increase in the area of the enlarged tube surpasses a definite bound, the stream from the nozzle exhausted into the suddenly expanded tube inclines to reattach at a reattachment distance greater than the optimal for a robust vortex in the recirculation zone. That affects the NPR's impact on base pressure, which is irrelevant at greater area ratios.

Fig. 11a shows the results for the duct segment L/D = 4; here, once again, the results for the lower rib heights are the same as those observed for earlier rib placements. The only difference is that, for a 2 mm rib height, there is a slight growth in base pressure for tube segments with L/D = 5 and 6. This increase can be attributed to the absence of backpressure, as ambient pressure has an insignificant impact on the base pressure for the tube segment with L/D = 4. It is also noted that for rib heights ranging from 3 mm to 5 mm, there is a substantial growth in base pressure at the earlier rib location (L/D = 2.0), with base pressure attaining values of 1.65, 2.5, and 4.0. There are marginal variations in the base pressure for pipe segments L/D = 5 & 6; the reasons for these variations have been discussed above.

4.7 Base Pressure Findings for Rib Position at L/D = 4.0

Fig. 12 shows the base pressure results for numerous NPRs, duct lengths, and rib altitudes when the rib is stationed at L/D = 4. From the results, it is seen that as far as small rib heights are concerned, the results are the same; however, for rib heights varying from 3 mm to 4 mm, a growth in the base pressure is seen, whereas for the maximum height of the rib, no change in the base pressure is seen. Results suggest that changes in base pressure for rib heights of 3 and 4 mm may be attributed to shock formation at M = 1.8. The interaction of the incident and reflected oblique shock waves, which is also influenced by the additional vortices created at the rib pointed corner, as seen in Fig. 12a. Similarly, the base pressure findings for the duct segment with L/D = 6 are shown in Fig. 12b and are constant. As discussed earlier, when the flow is connected to the duct, the base pressure results are independent of the length of the enlarged duct.

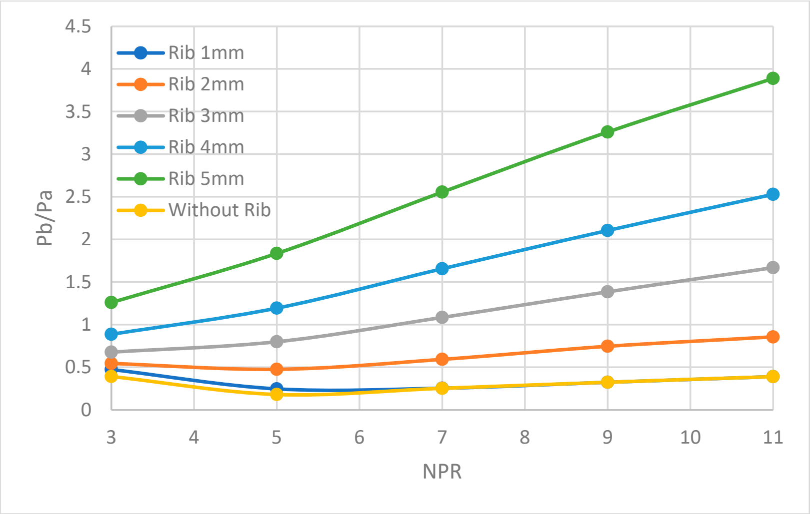

(**a**) L/D = 4

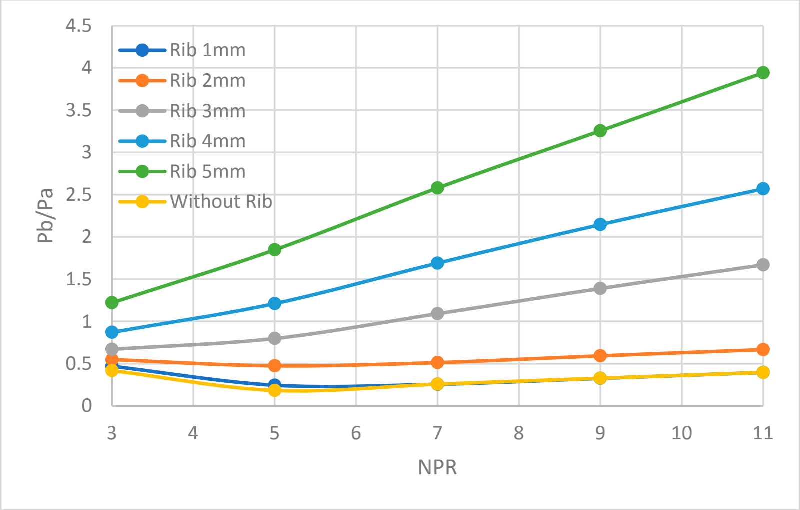

(**b**) L/D = 5

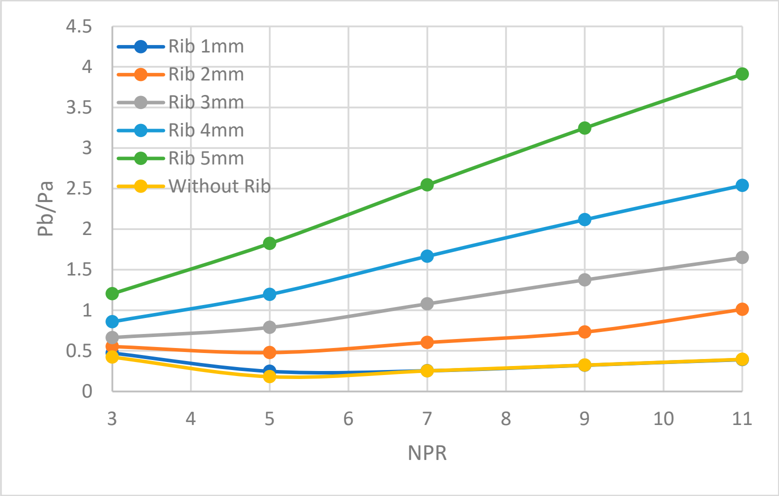

(c) L/D = 6

Figure 11: Base pressure ratio vs. NPR at different rib heights, rib location at L/D = 3.0, and the duct lengths. (**a**) L/D = 4, (**b**) L/D = 5, (c) L/D = 6.

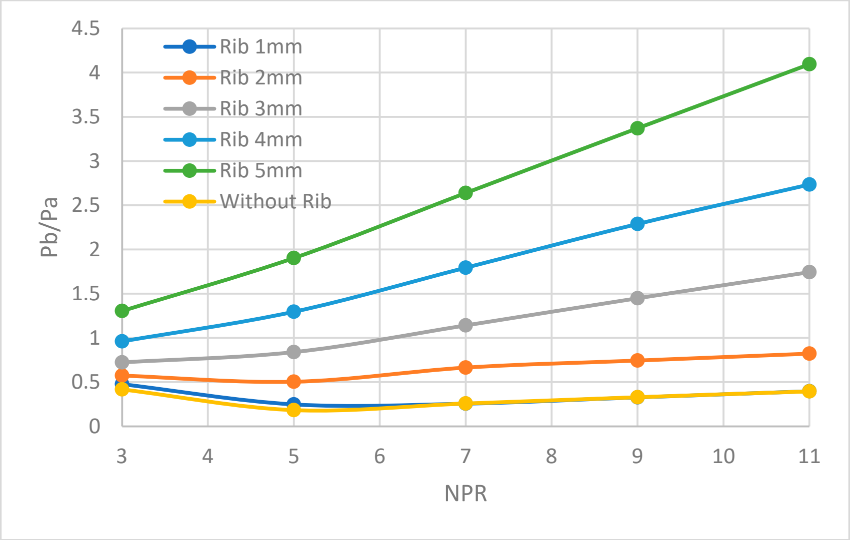

(**a**) L/D = 5

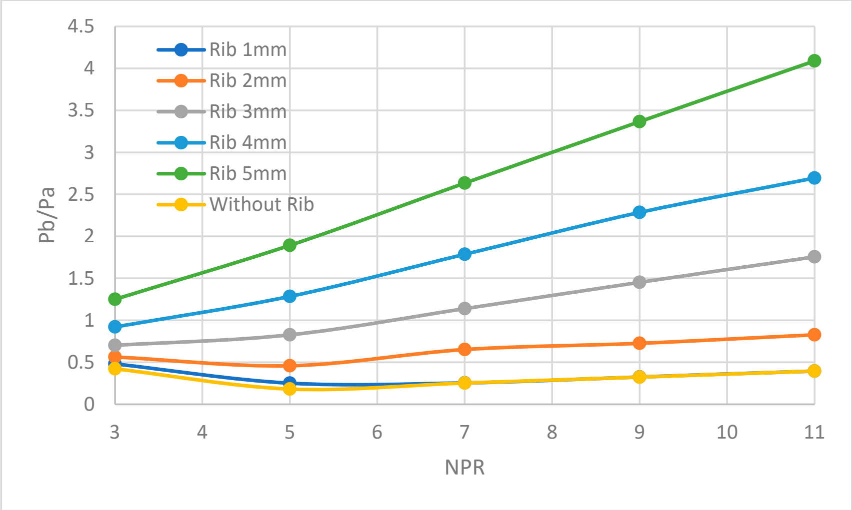

(**b**) L/D = 6

Figure 12: Base pressure ratio vs. NPR for various rib heights, rib location at L/D = 4.0, and the duct lengths. (**a**) L/D = 5, (**b**) L/D = 6.

5 Conclusion

Based on the above deliberations, we may conclude that:

- When the rib height is 1 mm, and the L/D is 0.5, the control is marginally effective, increasing the base pressure ratio from 0.4 to 0.6. For the remaining locations in the present study, the triangular rib with a height of 1 mm is ineffective, except for NPRs in the range of 3 to 6, where the nozzles pass through regions of either adverse or favorable pressure. Even within these NPR ranges, the rib's effectiveness is negligible.
- The triangular rib, with an altitude of 2 mm, is effective in reducing base suction, and its effectiveness is nearly the same for all the locations of the rib, except when stationed at L/D = 1.
- While the triangular rib height is 3 mm, the base pressure exceeds the back pressure. If the mission requirements call for maintaining a base pressure equal to backpressure, a rib height of 3 mm is

preferred. However, if users want to build the base pressure to 1.5 to 2.5 times the backpressure, ribs with heights of 4 mm and 5 mm are the right choice.

- A further increase in rib height results in higher base pressure, reaching extreme values of 2.7 and 4.0.
- Hence, we may conclude that these results are merely a technological demonstration. Dependent on the user's constraints, the final decision can be made on rib geometry, rib locations, duct size, and expansion level.

Acknowledgement: This research is supported by the Structures and Materials (S&M) Research Lab of Prince Sultan University.

Funding Statement: The authors acknowledge Prince Sultan University's support in paying the article processing charges (APC) for this publication.

Author Contributions: The authors confirm contribution to the paper as follows: Writing—original draft preparation, Abdul Aabid, Sher Afghan Khan; conceptualization, Ambareen Khan, Sher Afghan Khan; validation, Abdul Aabid, Renita Sharon Monis; resources, Muneer Baig; review and editing, Renita Sharon Monis, Sher Afghan Khan, Muneer Baig; evaluation, Muneer Baig. All authors reviewed and approved the final version of the manuscript.

Availability of Data and Materials: The data that supports the findings of this study are available from the corresponding author upon reasonable request.

Ethics Approval: Not applicable.

Conflicts of Interest: The authors declare no conflicts of interest.

Nomenclature

A_1	Nozzle Exit Area
A_2	Duct Exit Area
A_2/A_1	Area Ratio
M	Mach Number
L/D	Length-to-diameter Ratio
P_a	Atmospheric Pressure
P_e	Pressure at the exit of the nozzle
P_e	Pressure at the exit plane of the nozzle
ρ	Air Density
μ	Air Viscosity
μ_o	Reference Viscosity
T	Static Temperature
T_o	Reference Static Temperature (in K)
S	Sutherland Constant
k	Thermal Conductivity
C_p	Specific heat capacity
a	The velocity of sound
P_{inlet}	Inlet Pressure
P_{outlet}	Outlet Pressure
P_{gauge}	Gauge Pressure
P_o	Stagnation Pressure in the settling Chamber
P_b/P_a	Non-dimensional Base Pressure Ratio
P_e/P_a	Pressure Ratio at the nozzle to atmospheric pressure
NPR	Nozzle Pressure Ratio (i.e., P_0/P_a)
σk	Turbulent Prandtl number

ε	Turbulent kinetic energy dissipation rate
C_μ, C_1, C_2, f_μ, $\sigma\varepsilon$	Arbitrary Constant
v	Velocity
μt	Turbulent Viscosity
Prt	Turbulent Prandtl number
L	Length of the enlarged duct
D	Diameter of the enlarged duct
Di	Nozzle inlet diameter
w	Width of the rib
l	Length of the rib
h	Rib height
RAP	Reattachment point
RAL	Reattachment length

References

1. Pakhomov MA, Terekhov VI. Gas-droplet flow structure and heat transfer in an axisymmetric diffuser with a sudden expansion. J Appl Mech Tech Phy. 2020;61(5):787–97. [CrossRef].
2. Davletshin IA, Dushina OA, Mikheev NI, Shakirov RR. Heat transfer and flow structure in a plane diverging channel. Int J Heat Mass Transf. 2022;189:122744. [CrossRef].
3. Shakirov RR, Davletshin IA, Mikheev NI. Kinematic structure of flow and the heat transfer in flat diffuser and confuser channels. Thermophys Aeromech. 2022;29(5):759–64. [CrossRef].
4. Davletshin IA, Mikheev NI, Shakirov RR. Secondary flows in a flat diffuser and their significance for the formation of a turbulence field. Thermophys Aeromech. 2023;30(6):995–1011. [CrossRef].
5. Arabi A, Salhi Y, Zenati Y, Si-Ahmed EK, Legrand J. Experimental investigation of sudden expansion's influence on the hydrodynamic behavior of different sub-regimes of intermittent flow. J Petrol Sci Eng. 2021;205:108834. [CrossRef].
6. Arabi A, Salhi Y, Zenati Y, Si-Ahmed EK, Legrand J. A discussion on the relation between the intermittent flow sub-regimes and the frictional pressure drop. Int J Heat Mass Transf. 2021;181:121895. [CrossRef].
7. Arabi A, Salhi Y, Zenati Y, Si-Ahmed EK, Legrand J. Identifying the intermittent flow sub-regimes using pressure drop time series fluctuations. Exp Comput Multiph Flow. 2024;6(1):28–40. [CrossRef].
8. Arabi A, Abdul-Majeed GH, Boukrouche HB, Larbi Z. Pressure recovery model for gas–liquid two-phase flow across sudden expansions. Exp Comput Multiph Flow. 2024;6(1):14–27. [CrossRef].
9. Kopparthy S, Mansour M, Janiga G, Thévenin D. Numerical investigations of turbulent single-phase and two-phase flows in a diffuser. Int J Multiph Flow. 2020;130:103333. [CrossRef].
10. Golubkina IV, Osiptsov AN. Compressible gas-droplet flow and heat transfer behind a condensation shock in an expanding channel. Int J Therm Sci. 2022;179:107576. [CrossRef].
11. Salem KM, Elreafay AM, Abumandour RM, Dawood AS. Modeling two-phase gas-solid flow in axisymmetric diffusers using cut cell technique: an Eulerian-Eulerian approach. Bound Value Probl. 2024;2024:150. [CrossRef].
12. Pakhomov MA, Terekhov VI. Modeling of turbulent heat-transfer augmentation in gas-droplet non-boiling flow in diverging and converging axisymmetric ducts with sudden expansion. Energies. 2022;15(16):5861. [CrossRef].
13. Kim Y, Nam J, Roh TS, Lee HJ. Base flow and drag characteristics of a supersonic vehicle with cold and hot jet flows of nozzles. Aerospace. 2023;10(10):836. [CrossRef].
14. Lee S, Zhao Y, Luo J, Zou J, Zhang J, Zheng Y, et al. A review of flow control strategies for supersonic/hypersonic fluid dynamics. Aerosp Res Commun. 2024;2:13149. [CrossRef].
15. Rashid S, Nawaz F, Maqsood A, Salamat S, Riaz R. Review of wave drag reduction techniques: advances in active, passive, and hybrid flow control. Proc Inst Mech Eng Part G J Aerosp Eng. 2022;236:2851–84. [CrossRef].
16. Khan A, Mazlan NM, Sulaeman E. Effect of ribs as passive control on base pressure at sonic Mach numbers. CFD Lett. 2022;14(1):140–51. [CrossRef].
17. Khan A, Ismail MA, Mazlan NM. Numerical simulation of suddenly expanded flow from converging nozzle at sonic Mach number. In: Proceedings of International Conference of Aerospace and Mechanical Engineering 2019; 2019 Nov 20–21; George Town, Malaysia. [CrossRef].

18. Ali Baig MA, Al-Mufadi F, Khan SA, Rathakrishnan E. Control of base flows with micro jets. Int J Turbo Jet Engines. 2011;28(1):59–69. [CrossRef].
19. Rehman S, Khan SA. Control of base pressure with micro-jets: part I. Aircr Eng Aerosp Technol. 2008;80(2):158–64. [CrossRef].
20. Rathakrishnan E. Effect of ribs on suddenly expanded flows. AIAA J. 2001;39:1402–4. [CrossRef].
21. Aabid A, Khan SA. Investigation of high-speed flow control from CD nozzle using design of experiments and CFD methods. Arab J Sci Eng. 2021;46(3):2201–30. [CrossRef].